

**Structure and properties of formaldehyde-free faba bean starch composite foams
influenced by additives and lignin-glyoxal co-polycondensation**

Kehinde James Falua, Ravi Patel, Mostafa Nikkah Dafchachi, Amin Babaei-Ghazvini, Bishnu Acharya*

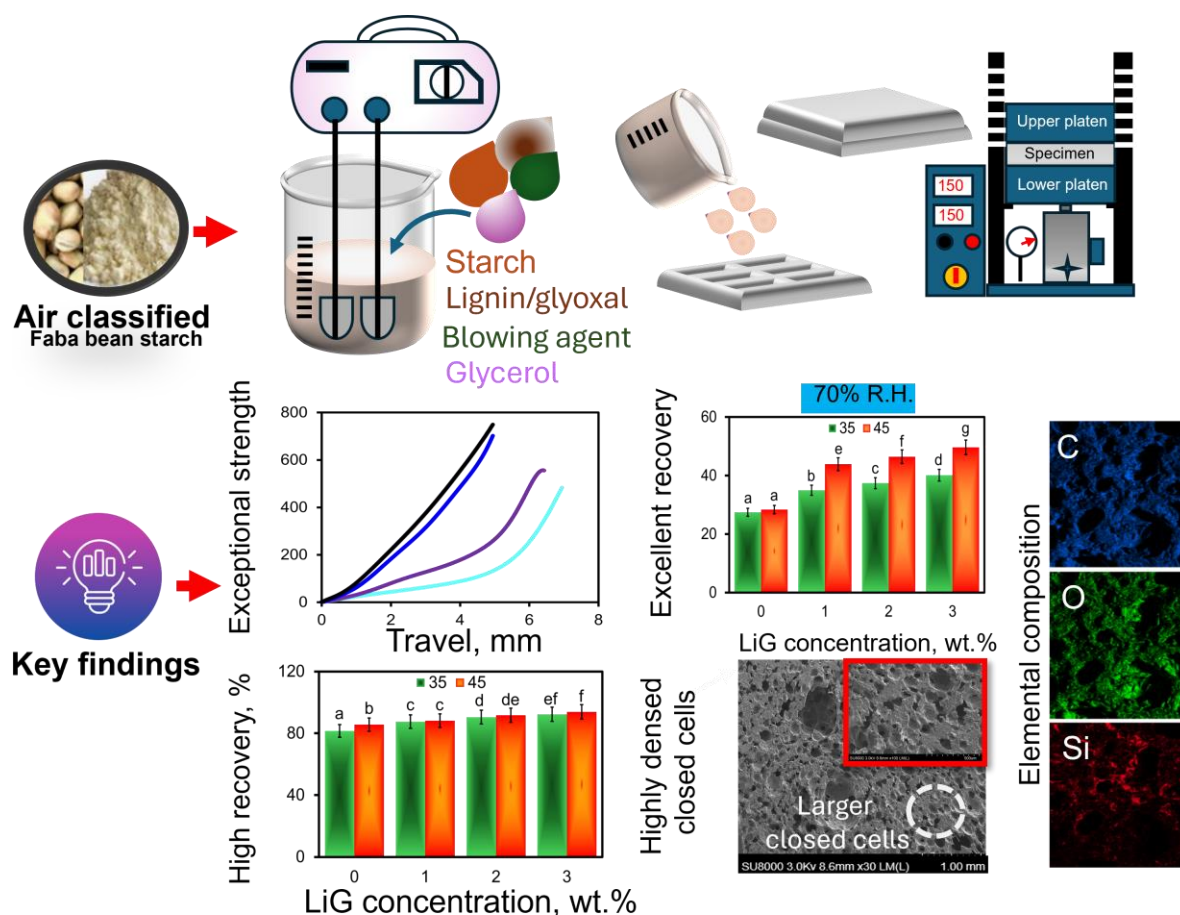
Department of Chemical and Biological Engineering, College of Engineering, University of Saskatchewan, Saskatoon, SK S7N 5A9, Canada

*Corresponding author: bishnu.acharya@usask.ca

Abstract

Highlights

Graphical abstract



1. Introduction

In recent decades, polymeric foams have gained considerable attention in various fields such as packaging, construction, and water treatment due to their exceptional properties, including lightweight, ultra-low density, low cost, and high impact resistance (Adebayo et al., 2024; Niu et al., 2023). Commercial foam materials are predominantly derived from precursors like polyols and isocyanates, which are also integral in the production of various plastics, such as polystyrene, polyethylene, and polyurethane (Chaudhary et al., 2024). However, the increasing generation of substantial waste volumes, coupled with restricted end-of-life disposal or recycling pathways and the worldwide implementation of plastic ban, underscores the urgent need for sustainable and eco-friendly alternatives to replace these petroleum-based foams (Glenn et al., 2023; Liao et al., 2024). Biomass such as starch, cellulose, lignin, hemi-cellulose has all emerged as excellent feedstocks for biofoam production with remarkable properties. Given their appealing environmental-friendly nature, starch from various plant materials has been widely used for in biofoam production. Starch biofoams typically exhibit a wide range of densities, characterized by significant specific surface area (SSA) and excellent thermal conductivity (Zheng et al., 2024). However, these properties are dependent on the type of fabrication techniques used.

Extrusion, hot-mold baking (compression molding), microwave heating, freeze-drying and super-critical fluid extrusion (SFE) have all been employed to produce biodegradable foams depending on targeted applications. Biodegradable foams produced through supercritical fluid extrusion (SFE) techniques exhibit highly porous structures, making them particularly suitable for advanced applications such as tissue engineering scaffolds and drug delivery systems

(Carrascosa et al., 2024; Zhou et al., 2024)). In contrast, compression molding is widely preferred for applications like cushioning and packaging due to its ability to produce lightweight foams with adequate strength. However, not all of the aforementioned fabrication techniques are viable for large-scale production, as they often involve significant energy and time requirements, as well as the need for specialized training (Liao et al., 2024; R. Wang et al., 2022). Compression-molded foams offer rapid production and facilitate the creation of precise, desired shapes. In the context of starch-based foams, the composition of amylose and amylopectin in the starch significantly impacts their properties. Foams derived from high-amylose starch exhibit greater strength and density compared to those made from high-amylopectin starch, which are typically less dense and mechanically weaker. Han et al. (2023) systematically evaluated the foaming behavior, as well as the thermal and mechanical properties, of biofoams produced from waxy corn starch and high-amylose corn starch. Their results revealed that biofoams made with high-amylose starch displayed higher density, superior flexural strength, reduced water absorption, but irregular cell structures. Starch-based foams face notable challenges due to the inherent high hydrophilicity of starch and its limited mechanical integrity.

Extensive studies have highlighted the compatibility of starch with cellulosic or lignocellulosic fibers, natural rubbers, and proteins, which can provide mechanical reinforcement and enhance water resistance. Despite these advancements, research by Phiriyawirut et al. (2022) and Moo-Tun et al. (2020) revealed that while incorporating fibers such as chitosan, jute, corn stalk, and sugarcane bagasse into starch foams improves mechanical properties, it does not significantly enhance water resistance. For this reason, lignin, accounting for 20–30% in lignocellulosic biomass (Toledano et al., 2012), has gained attention for its potential in reinforcing porous phenolic foams, aerogels, and other composite materials. Historically utilized in energy applications, lignin's scope has expanded due to advancements in thermochemical conversion techniques that enable the production of low-molecular-weight lignin (B. Li et al., 2017, 2019; Mahmood et al., 2016). These developments have broadened lignin's usefulness, particularly in biofoam formulations, where it offers promising prospects for addressing water resistance challenges. Recently, Adebayo et al. (2024) synthesized biobased lignin-furan foams. Their results indicated closed cells cellular morphology with cell diameter range from 10 to 200 μm . Also Li et al. (2019) developed new foaming formulations through synthesis of bio-phenol formaldehyde (BPF) using kraft lignin. Findings from their results revealed that the BPF/lignin foams demonstrated strong compressive strength around 1 MPa. Few reports also developed starch-lignin biofoams. For instance, (Kustiyah et al., 2019) added lignin into starch-cellulose biofoams to produce hybrid closed cells polyurethane foams. Likewise, corn starch-kraft lignin foams manufactured via compression molding showed comparable flexural strength to foamed polystyrene (E. S. Stevens et al., 2010). Cellulose fiber foams manufactured by compression molding indicated exceptionally high porosity (95 to 99.6%) and densities ranged from 0.0062 to 0.075 g/cm^3 (Glenn et al., 2023). Similarly, lignin-furan based biofoams showed maximum thermal degradation between 453 $^{\circ}\text{C}$ and 457.4 $^{\circ}\text{C}$ (Adebayo et al., 2024). To the best of our knowledge, research work investigating lignin-glyoxal interaction as formaldehyde-free agent in high-amylose starch foams is less reported. This further amplifies the novelty of this present study.

It is worth noting that the decades' use of traditional wood-based adhesives such urea-or-melamine-formaldehyde has been found to be one of the primary causes of harmful emissions, triggering the search for natural resin adhesives (Xu et al., 2025). Glyoxal owing to its low toxicity, easy biodegradation, and low volatility is considered as an ideal replacement for formaldehyde (Siahkamari et al., 2022). Interestingly this unique natural material has potential usefulness in the biomedical field and could serve as a curing or crosslinking agent in foams (Farouk et al., 2022; Lee & Park, 2023). However, limited crosslinking density could arise due

to its small bifunctional aldehyde reacting with hydroxyl groups in polymers. Different materials such as urea (Deng et al., 2014; Younesi-Kordkheili, 2017), melamine (M. Liu et al., 2023; Xu et al., 2025), etc. have been synthesized with glyoxal. Lignin lacks sufficient aldehyde functionality to act independently as an effective crosslinking agent. However, when glyoxal interacts with lignin's reactive sites through co-polycondensation, it forms a robust and intricately interconnected polymer network. Herein, this study investigates the structure and properties of foams develop using high amylose faba bean starch influenced by the additives and lignin-glyoxal interaction based on density, porosity, mechanical strength, SEM, FT-IR, and TGA. Meanwhile, this research offers a novel eco-friendly approach for the advancement of formaldehyde-free starch-foams, bolstering their potential application across different industries.

2. EXPERIMENTAL DETAILS AND CHARACTERIZATION

Faba bean starch-rich flour (Homecraft® 3103) was supplied by AGT Food and Ingredients (Saskatoon, SK, Canada). The starch-rich flour is a co-product derived from fractionated dehulled faba bean seed using the air classification technology. To preserve its powdery texture and prevent moisture absorption, the flour was stored at room temperature prior to use in the experiments. Based on the supplier's information sheet, the starch and protein contents were 65.3% and 20.2%, respectively. Chemicals, including sodium bicarbonate (Na_2CO_3), magnesium nitrate hexahydrate ($\text{Mg}(\text{NO}_3) \cdot 6\text{H}_2\text{O}$), glyoxal, and glycerol were purchased from Sigma-Aldrich Inc. (Ontario, Canada). Beeswax, used as a mold release agent, was purchased from a local supplier. Distilled water was used in the batter preparation. All the reagents used in this research were of analytical grade, ensuring high-quality experiments and reliable results.

In the dough preparation, air classified faba bean starch (FBS) (35 or 45 g) was dissolved in 25 mL of distilled water and homogenized using a kitchen stand mixer (BettyCrocker™ BC-3220CMR, China) equipped with a stainless-steel rod whisk attachment for 7–10 min. Na_2CO_3 (3% of the starch weight) was added as a blowing agent, while glycerol (20% of the dry starch weight) was incorporated to enhance plasticization, followed by further stirring to ensure homogenous blending of all components. A lignin:glyoxal (LG) mixture, consisting of glyoxal (40 wt.%), and soda lignin powder extracted from wheat straw in a 1:3 ratio (based on the molecular weight of their functional groups), was then introduced into the starch dough and stirred at the maximum speed for an additional 3 min. To improve the viscosity of the starch dough, an additional 5 mL of distilled water was added during the mixing. During the process, fragments of the starch dough retained on the inner wall of the mixing container were periodically wiped down using a spatula to ensure consistent mixing.

A stainless steel mold (230 mm × 230 mm × 30 mm) with six cavities, each measuring 50 mm × 10 mm × 15 mm was used in the compression molding process. The engineering drawing is provided in **Figure S1**. Each cavity was overfilled (135%) before placing the upper part of the mold to ensure creation of sufficient flow pressure and fill void spaces during expansion (Glenn et al., 2023). We utilized a compression molder (Carver, Model 4389, Carver Inc., IN, USA), embedded with a hydraulic unit (Model 3925) having a maximum ram stroke of 6 1/2' for the molding process. The upper and lower platens were first preheated to 150 °C before the mold was placed between them. The space between the platens was adjusted using the hydraulic unit. This facilitates the platen-mold grip for at least 3 min molding process. After that, the hydraulic unit was released, and the mold was carefully removed and allowed to cool for at least 30 min. Finally, the biofoam was gently removed from the cavities prior to conditioning at 55% RH for 24 h prior to further testing. Table 1 outlines the dough components, and their proportions used for the biofoam synthesis, along with a control sample for comparison.

Table 1: Faba bean starch-based biofoam formulation with varying starch and lignin-glyoxal ratios

Biofoams	Starch (g)	LG (g)	Na ₂ CO ₃ (g)	Water (g)	Glycerol (g)	Total mass (g)	LG (wt.% of dry starch)
S ₃₅ LiG ₀	35	0	1.75	30	7	73.75	0
S ₄₅ LiG ₀	45	0	2.25	30	9	86.25	0
S ₃₅ LiG ₁₀	35	0.35	1.75	30	7	74.10	1.0
S ₄₅ LiG ₁₀	45	0.45	2.25	30	9	86.70	1.0
S ₃₅ LiG ₂₀	35	0.70	1.75	30	7	74.45	2.0
S ₄₅ LiG ₂₀	45	0.90	2.25	30	9	87.15	2.0
S ₃₅ LiG ₃₀	35	1.05	1.75	30	7	74.80	3.0
S ₄₅ LiG ₃₀	45	1.35	2.25	30	9	87.6	3.0

The apparent density of the biofoams was calculated based on the dry mass and the length, width, and thickness of each tested specimen according to IS EN ISO 845:2006 as expressed in equation 1.

$$\rho = \frac{m}{l \times w \times h} \quad (1)$$

Where l , w , and h are the foam's length (mm), width (mm), and thickness (mm), respectively.

The compressive strength of the conditioned samples was tested using a motorized tension/compression stand (Mark-10 ESM 303, ITM Instruments Inc., NY, U.S.A.), applying force along tangential and radial directions. A 1 kN load cell was employed, and the compression rate was set to 50 mm/min. The test was terminated when the compression strain reached 80% of the initial height. Both tangential and radial orientations of the biofoam specimens were assessed, and their mechanical properties were determined from the stress-strain curves. The tangential ultimate compressive strength (UCS) was identified as the maximum stress value at the onset of densification. In contrast, since the strength on the radial stress-strain response lacked a distinct plateau, the UCS in this direction was determined from the final recorded stress value. The resilience of the biofoams in the radial (Z) direction was estimated as the percentage shape recovered after compression.

The impact test was conducted using unnotched biofoam specimens following ASTM D256-2010 procedure, using an Izod Impact Tester (Model DH-1843-5.5D, Dongguan Hongtuo Instruments Co. Ltd, Guangdong, China). Calibration was carried out at the beginning of the test series and repeated after each specimen to ensure consistent machine accuracy. Friction loss was stable throughout the tests, remaining at approximately 0.28% of the pendulum energy (5.5 J). For each test, the pendulum was raised to its default angle (150°), securely latched, and clamped for safety. The dimensions of the unnotched specimens were 57.72 mm × 13.12 mm × 9 mm was input into the equipment, and each specimen was gently secured in the clamping vise. The pendulum was then released to strike the specimen, and the impact resistance was recorded directly from the tester's monitor display. A minimum of 15% residual energy is required at the conclusion of each test (Patterson et al., 2019). In this study,

the energy level was suitable for all tested materials, with the average impact resistance of the specimens measured at 63% of the pendulum's total energy.

The moisture uptake was calculated according to procedure highlighted in (Ago et al., 2016), with slight modification. Biofoam specimens, were conditioned at $70 \pm 4\%$ relative humidity at $24\text{ }^{\circ}\text{C}$ in a desiccator. The weight of foams was monitored intermittently every 6 h until a steady value was obtained and the moisture uptake was calculated using Equation 3 as

$$\text{Moisture uptake (\%)} = \frac{W_2 - W_1}{W_1} \quad (3)$$

Where W_1 and W_2 are the mass of the sample before and after water sorption respectively. The experiment was carried out in triplicate and average values reported.

Thermogravimetric analysis (TGA) of the biofoams was performed to determine the thermal behavior of the composite biofoams. Using a thermogravimetric (TG) analyzer (TGA 8000TM, PerkinElmer[®], Ontario, Canada), ~10 mg of the biofoam was heated from $50\text{ }^{\circ}\text{C}$ to $800\text{ }^{\circ}\text{C}$ at a heating rate of $50\text{ }^{\circ}\text{C}/\text{min}$, under a nitrogen inert atmosphere of $30\text{ mL}/\text{min}$. The mass loss in the samples was plotted as a function of weight loss with respect to temperature. The decomposition temperature was determined from the peak of the derivative curves using OriginPro 2023b Software v. 10.0.5.153.

The intrinsic structure of the composite foams indicating their interconnectivity and pore distribution was examined using a field emission scanning electron microscope (FESEM, SU8010, Hitachi High Technologies Canada Inc., Rexdale, Ontario, Canada), equipped with energy-dispersive X-ray spectroscopy (EDS). The SEM was operated at an accelerating voltage of 3.0 kV and a current of 10 A . Elemental composition within the biofoam specimens was analyzed using the EDS system, employing AztecLiveStandard software with an Ultim Max 170 Detector. Approximately 1 mg of each foam sample was mounted on an aluminum stub using double-sided carbon adhesive tape. To prevent charging and enhance imaging quality, the samples were sputter-coated with a thin layer of gold. Micrographs were captured at various magnifications to ensure detailed observation. The infrared spectroscopy of the biofoams was performed using a Universal Attenuated Transmission Reflectance–Fourier Transform Infrared (UATR–FTIR) (Spectrum 3 Tri-Range MIR/NIR/FIR Spectrometer, PerkinElmer, USA) with the spectra captured in the wavenumber range between $4000\text{--}400\text{ cm}^{-1}$.

All experimental data were analyzed using a completely randomized design with a one-way analysis of variance (ANOVA) in the Statistical Package for Social Sciences (SPSS) software (Version 28.0.1.0 (142); SPSS Inc., USA). Duncan's Multiple Range Test (DMRT) was employed for mean comparisons at a 5% significance level.

3. RESULTS AND DISCUSSION

3.1. Mechanical performance and density

The biofoams were evaluated for their mechanical properties in both the tangential and radial orientations, as summarized in Table 1. Corresponding stress-strain curves (Figure 1a-d) reveal that all the specimens exhibited linear elasticity in the low-strain region, followed by a plateau indicative of plastic deformation, mostly evident in the tangential direction. In contrast, the radial direction lacked distinct plastic and densification zones, suggesting a gradual pore collapse rather than unique phase transitions. This observation further confirms the heterogeneity of void spaces within the biofoams microstructure. Among the tested formulations, $\text{S}_{45}\text{LiG}_{30}$ demonstrated the highest compressive strengths: 144.79 kPa in the tangential and 749.47 kPa in the radial orientations, suggesting superior resistance to deformation. Conversely, $\text{S}_{35}\text{LiG}_0$ displayed the lowest mechanical strengths, 29.23 kPa and

220.07 kPa in those directions. Structurally, biofoams consist of cell walls and cell edges with varying degrees of thicknesses, which undergo progressive cellular compression under stress (Borrero-López et al., 2022; Pagliocca et al., 2022). Initially, the cells deform elastically, followed by densification at higher loads, ultimately resulting in permanent plastic deformation. The inferior performance of $S_{35}LiG_0$ can be attributed to the absence of LiG reinforcement, leading to a polymer matrix dominated by soft, flexible segments that lack sufficient load-bearing capacity. Consequently, these biofoams collapsed under compression and experienced large strains immediately after the plateau region, supported by previous reports (Ago et al., 2016; Liao et al., 2024). Biofoams synthesized from PLA-blended corn starch (25% amylose and waxy starch) exhibited compressive strengths between 90 and 270 kPa (Fang & Hanna, 2000). Additionally, cellulose nanofibrils in amylopectin-based foams have been shown to enhance both yield stress and Young's modulus, underscoring the role of crystalline packing and reinforcement on composite foam mechanical properties (Ago et al., 2019). Regardless of starch weight and biofoam orientation, Young modulus (YM) increased with LiG concentration, highlighting its crucial role in enhancing the biofoam stability. Differences in the YM between the tangential and radial directions suggest anisotropic structural reinforcement, likely influenced by molecular interactions and pore morphology (De Carolis et al., 2024; Lu et al., 2021; Obradovic, 2017; Vo et al., 2020). Further observation revealed that while the stiffness of the biofoams increased, specific Young's modulus (SYM) declined significantly with higher LiG concentration. This is because LiG introduces additional mass into the foam structure, offsetting the stiffness gains when normalized by density. Additionally, higher SYM in the tangential direction could be ascribed to the non-uniform cell wall, likely facilitating a more effective load transfer. Among all formulations, $S_{45}LiG_{10}$ exhibited the highest SYM ($78.74 \text{ MPa}\cdot\text{g}^{-1}\cdot\text{cm}^3$), whereas $S_{35}LiG_{20}$ had the lowest ($12.21 \text{ MPa}\cdot\text{g}^{-1}\cdot\text{cm}^3$). The ability of biofoams to withstand sudden loading were evaluated under two environmental conditions: 0% and 70% relative humidity (RH) (Figure 1g-h). At 0% RH, biofoams formulated with lower starch content (S_{35}) exhibited impact resistance values between 25.30 to 36.39 J/m, while the higher-starch-content biofoams (S_{45}) had values ranging from 27.68 and 47.35 J/m. These values were notably lower than those obtained at 70% R.H. The presence of moisture at 70% RH acts as a plasticizer, enhancing polymer chain mobility, increasing flexibility, and allowing for greater deformation and energy dissipation during impact (Mathew et al., 2008; Saini et al., 2024). Conversely, at 0% RH, the absence of moisture promotes brittleness, limiting plastic deformation. Biofoams with higher starch content (S_{45}) consistently demonstrated superior resistance to external forces due to a denser, more cohesive matrix (Bergel et al., 2021; Machado et al., 2017). For reference, (Kaewtatip et al., 2018) reported impact resistance range between 0.28 and 0.69 J/m for cassava starch foams mixed with commercial calcium carbonate, shrimp shell, and eggshell powder, conditioned at 78% RH. Similarly, potato starch foams reinforced with treated cotton fibers exhibited increased impact resistance (12.69–66.52 J/m) compared to untreated foams (12.33 kJ/m), although they remained less robust than foams with normal cotton microfibers (11.95–34.35 J/m) (Bergel et al., 2021). These variations are likely due to differences in specimen composition or thickness, and testing conditions, such as pendulum energy. In this study, the highest impact resistance was observed in specimens with higher LiG concentration (3 wt.%), demonstrating the benefits of optimal crosslinking density and improved interfacial bonding within the starch matrix. In contrast, biofoams without LiG exhibited the lowest impact resistance, regardless of starch content (S_{35} or S_{45}), suggesting insufficient matrix cohesion. Density is a crucial parameter in applications such as packaging (Duan et al., 2022). As seen in Figure (1i), FBS foam apparent densities range from 0.60 to 0.97 g/cm^3 for S_{35} formulations and 0.67 to 1.25 g/cm^3 for S_{45} formulations. Apparent density generally increases with LiG concentration, indicating enhanced structural reinforcement. Prior studies have demonstrated that high amylose starches

yield foams with higher densities (Finkenstadt et al., 2016; Soykeabkaew et al., 2015; Willett & Shogren, 2002). The densities reported here are significantly higher than those of extruded starch/poly vinyl alcohol (PVA) foams (0.017–0.027 g/cm³) (F. Liu et al., 2025), extruded corn starch foams (0.019–0.033 g/cm³) (Duan et al., 2022), and amylopectin waxy corn starch with NaOH-treated fruit branch fibers 0.091 g/cm³ (Ago et al., 2016). Factors such as fabrication technique, starch type, batter formulation, moisture content, filler type and concentration, and starch weight contribute to these differences. Higher densities in the S₄₅ formulations reflect greater starch availability for crosslinking and reduced porosity, as supported by prior studies (Amaraweera, Gunathilake, Gunawardene, Dassanayake, Fernando, Wanninayaka, Rajapaksha, Manamperi, Gangoda, Manchanda, et al., 2022; Carvalho et al., 2025; Suwandecha & Pisuchpen, 2024). The percentage recovery of the biofoams (Figure 1j) further substantiates the observed mechanical trends. Linear correlation exists between LiG concentration and recovery rate, with S₄₅LiG₃₀ exhibiting the highest percentage recovery (93.89%), whereas S₃₅LiG₀ indicating the lowest recovery (81.59%). Biofoams with higher structural integrity exhibit minimal permanent deformation upon unloading. Although few recent studies have documented recovery percentages ranging from 70% to 92.5% ((Georges et al., 2018; F. Liu et al., 2023; Pan et al., 2023)), recovery of composite foams, however, could be directly influenced by homogeneity of the cell structure, foaming ratio, and other modification or formulation techniques.

Table 1: Mechanical properties for biofoams obtained from air classified starch with lignin:glyoxal at given loading of LiG (0%, 1%, 2%, and 3%)[†].

Biofoam specimen	UCS _T (kPa)	YM _T (kPa)	SYM _T (MPa.g ⁻¹ .cm ⁻³)	UCS _R (kPa)	YM _R (kPa)	SYM _R (MPa.g ⁻¹ .cm ⁻³)	Recovery (%)
S ₃₅ LiG ₀	29.23±0.91 ^a	8.81±0.20 ^a	68.05±0.72 ^{de}	220.07±2.64 ^a	14.89±0.40 ^a	40.30±2.14 ^e	89.59±1.10 ^a
S ₄₅ LiG ₀	33.41±0.63 ^b	11.33±1.23 ^b	59.29±5.74 ^{cd}	483.16±8.63 ^e	22.24±1.72 ^b	30.11±1.93 ^d	85.65±1.34 ^b
S ₃₅ LiG ₁₀	53.75±1.57 ^c	9.95±1.07 ^a	70.55±10.22 ^{ef}	335.13±2.90 ^b	46.16±1.86 ^d	15.09±1.24 ^{ab}	87.53±1.43 ^c
S ₄₅ LiG ₁₀	57.73±1.47 ^d	12.90±0.13 ^c	78.74±8.81 ^f	555.52±6.43 ^f	31.73±1.73 ^c	32.01±3.20 ^d	88.20±0.28 ^c
S ₃₅ LiG ₂₀	89.56±1.65 ^f	16.98±0.89 ^d	44.10±3.30 ^b	387.43±0.85 ^c	61.22±1.25 ^d	12.21±0.59 ^a	90.48±0.91 ^d
S ₄₅ LiG ₂₀	84.64±0.68 ^e	19.64±0.67 ^e	57.86±2.36 ^c	702.25±0.93 ^g	58.99±0.23 ^d	19.24±0.25 ^c	91.70±0.42 ^{de}
S ₃₅ LiG ₃₀	108.67±0.35 ^g	39.92±0.12 ^g	24.27±0.61 ^a	443.63±0.80 ^d	67.15±0.34 ^e	14.43±0.29 ^a	92.30±1.20 ^{ef}
S ₄₅ LiG ₃₀	144.79±0.89 ^h	24.05±0.51 ^f	52.07±2.82 ^{bc}	749.47±1.34 ^h	70.55±1.44 ^f	17.75±0.94 ^{bc}	93.89±0.36 ^f

[†]Mechanical properties were obtained in compression mode. The data are reported as mean ± standard deviation (n=3). Columns with same alphabets are not significantly different ($P<0.05$). UCS: Ultimate compressive strength; SYM: Specific Young's modulus; *t* and *r* represent tangential and radial orientations, respectively.

3.2. Thermal stability and water absorption

TGA tests unravel the decomposition influenced by the kinetics (weight loss vs. temperature) of chemical reactions in composite materials (Dewi et al., 2024). As seen in Figure 2a, the thermal degradation profile of the composite foams exhibited two primary degradation steps, consistent across all formulations, indicating existential endothermic process. The first degradation step, occurring below 200 °C, was attributed to the release of volatiles, primarily residual moisture and glycerol (Falua et al., 2023; Gil-Guillén et al., 2025; Liang et al., 2024). This stage represents the evaporation of low molecular weight components and trapped volatiles within the starch matrix. Beyond this stage, the samples experienced approximately 60% weight loss in the temperature range of 240–370 °C, predominantly associated with the starch decomposition. Interestingly, increasing the LG concentration did not significantly alter the thermal decomposition onset of thermal decomposition or the maximum degradation temperatures. However, specimens without LiG decomposed more rapidly. This suggests that LiG imparted some degree of thermal stability within the foam structure, likely through its crosslinking effects (Fazeli et al., 2024; Iswanto et al., 2024; Joseph et al., 2024). Further insights were provided by the derivatives TGA curves (Figure 2b). S₃₅LiG₀ specimen exhibited more intense peaks in the 100–200 °C temperature range, indicating more volatile compounds within the starch matrix. Less intense peaks around this temperature range, mostly recorded in specimens incorporated with LiG underscores the effect of the LiG in reducing the moisture content and potentially forming a denser crosslinked network within the foam matrix. Enhanced interaction slows down thermal breakdown of composite structure. Fiber-reinforced rice starch composite foams had less peaks, indicating improved thermal stability (Quilez-Molina et al., 2024). Water sorption (WS) is an important parameter affecting biofoam applications, particularly in humid environments. The analyzed WS is summarized and presented in Table S1. WS values in this study ranged from 1.79% to 12.16%, dependent on starch content (S₃₅ or S₄₅) and the LiG concentrations (0, 1, 2, and 3 wt.%) in the biofoams. While similar WS values have been reported by (Ago et al., 2016), (Duan et al., 2022), and (Dewi et al., 2024), it is widely reported that factors such as crosslinking density, matrix structure, plasticizing effects, relative humidity, and available hydrophilic sites play crucial roles in determining water absorbed (Duan et al., 2022; Qiu et al., 2021; S. Wang et al., 2024; X. Zhang et al., 2024). It could be observed that S₃₅LiG₃₀ exhibited the lowest initial water absorption (1.79% on day 1), which gradually increased to 8.31% by day 7. This initially low moisture uptake can be attributed to the reinforcing effect of lignin, which reduces the

availability of hydrophilic sites for moisture absorption (DSouza et al., 2024; Tang et al., 2024). However, prolonged exposure to moisture likely induced partial hydration and an irreversible collapse of porosity in the porous starch matrix, consistent with previous studies (Amaraweera, Gunathilake, Gunawardene, Dassanayake, Fernando, Wanninayaka, Rajapaksha, Manamperi, Gangoda, & Manchanda, 2022; Capezza et al., 2019; Digaitis et al., 2022; E. Stevens, 2010). $S_{35}LiG_{10}$ showed highest water absorbed ($\sim 10\%$) between days 2 and 4. This behavior suggests moderate crosslinking density, which allows water molecules to penetrate the foam matrix while still retaining sufficient hydrophilic sites for bonding. Insignificant differences observed in absorbed water in $S_{35}LiG_{30}$ and $S_{45}LiG_0$ specimens on days 5 and 6 could be attributed to saturation of their hydrophilic sites or delayed water uptake facilitated by open matrix structure within the specimens. In S_{35} formulations, increasing LiG concentration up to 3 wt.% initially increased the water absorption, but a further increase reduces the absorption before a final increase at 3 wt.% LiG, indicating molecular interactions between the starch matrix and the formulation components. Similarly, higher LiG concentrations initially restricted WS due to denser matrices in the S_{45} formulations, but gradual water absorption was observed over the testing period.

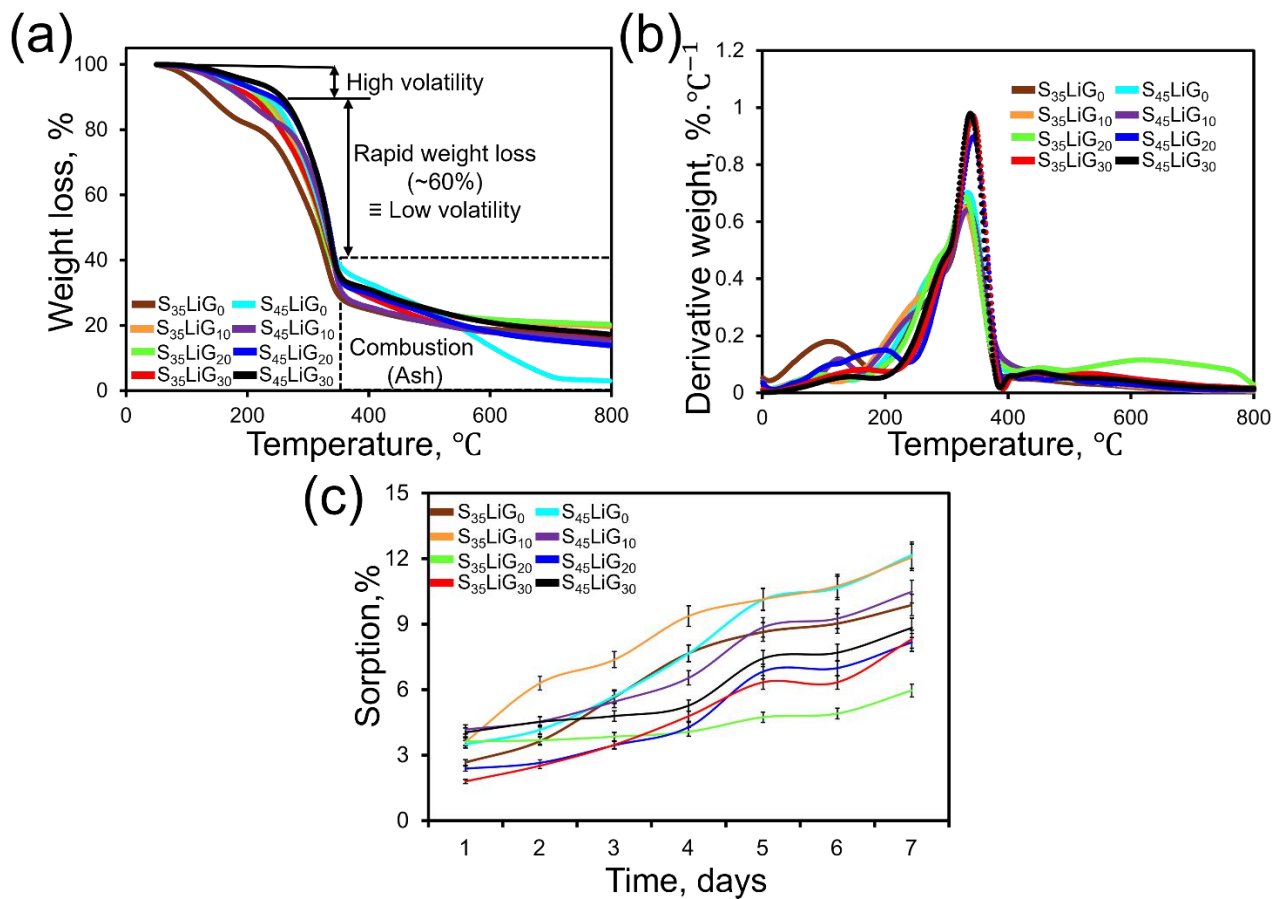


Figure 2:

3.3. UATR–FTIR and diffractograms analysis

The functional group analysis using UATR–FTIR was performed to identify the functional groups present in the biofoam specimens. The infrared spectra exhibited a strong band in the range of $3500\text{--}3000\text{ cm}^{-1}$, corresponding to O–H stretching vibrations (Figure 3a).

Additionally, stretching vibrations of C-H bonds were observed at 2925 cm^{-1} , while peaks at 1639 cm^{-1} and 1548 cm^{-1} were attributed to bending vibrations of adsorbed water and stretching vibrations of CH_2 groups, respectively (Quilez-Molina et al., 2022, 2024). Strong absorption bands near 1010 cm^{-1} were associated with the stretching vibrations of C–O and C–O–C bonds (Falua et al., 2025; Quilez-Molina et al., 2024). Further observations revealed that functional groups arising from lignin and glyoxal, which were incorporated into the biofoams, did not produce distinct or detectable peaks in the FTIR spectra. Sometimes, spectra of composite materials do not exhibit considerable differences due to interfacial adhesion between nanoparticles (Falua et al., 2025; C. Han et al., 2024; R. Liu et al., 2023; Viswanathan et al., 2024). Additionally, lignin and glyoxal contain functional groups such as hydroxyl and carbonyl groups, which overlap with starch in the FTIR spectra, potentially masking their individual contributions. The primary interaction between glyoxal and starch involves crosslinking through the aldehyde groups of glyoxal and the hydroxyl groups of starch (Chen et al., 2022; Ni et al., 2019). This reaction likely alters the molecular structure rather than introducing new functional groups, which might explain the absence of significant changes in the spectra observed in the foam specimens (Figure). Furthermore, the homogeneous dispersion of lignin and glyoxal within the starch matrix results in their functional groups interacting with starch hydroxyl groups through hydrogen bonding or crosslinking. These interactions can lead to subtle changes in peak intensities or minor shifts that are not readily distinguishable with FTIR. The diffractograms of the foam specimens revealed distinct crystalline peaks and peak shifts, providing insights into their structural organization (Figure 3c). The diffraction patterns displayed a characteristic type C pattern, which is typically associated with legume-based starches. This pattern featured intense diffraction peaks at approximately 16.72° , 19.86° , and 21.62° (2θ), aligning with the crystalline regions of starch granules. Although peaks at approximately 5.6° , 15° , and 23° have been previously reported in literature (Ambigaipalan et al., 2011; Suárez-Diéguez et al., 2021), the observed peak near 20° in this indicates the presence of V-type amylose crystallization complexes, likely formed during the compression molding process, in tandem with previous reports (Duan et al., 2022; Finkenstadt et al., 2016). Furthermore, it is observed that the crystalline structures within the starch foams were significantly disrupted, as evidenced by pronounced amorphous scatterings in the diffractograms. This disruption is expected, given that the baking temperature (150°C) exceeded the melting temperatures of starch crystalline regions (approximately between 61°C and 78°C) determined with differential scanning calorimetry (DSC) endotherms (D. Li et al., 2022; Nilsson et al., 2022; Z. Zhang et al., 2019). This elevated baking temperature likely resulted in the breakdown of organized crystalline regions, promoting amorphization within the foam matrix. Interestingly, the addition of LiG at specific concentrations appeared to influence the specimen's crystallinity. At lower concentrations (1-2 wt.%), the peaks in $\text{S}_{45}\text{LiG}_{10}$ specimen significantly reduced, only retaining diffraction at 19.86° . However, higher LiG (3 wt.%) markedly displayed the reappearance of the three distinct peaks. This suggests that LiG concentrations may facilitate the formation of crystalline regions by stabilizing the foam matrix and promoting interactions that reinforce the starch crystalline network.

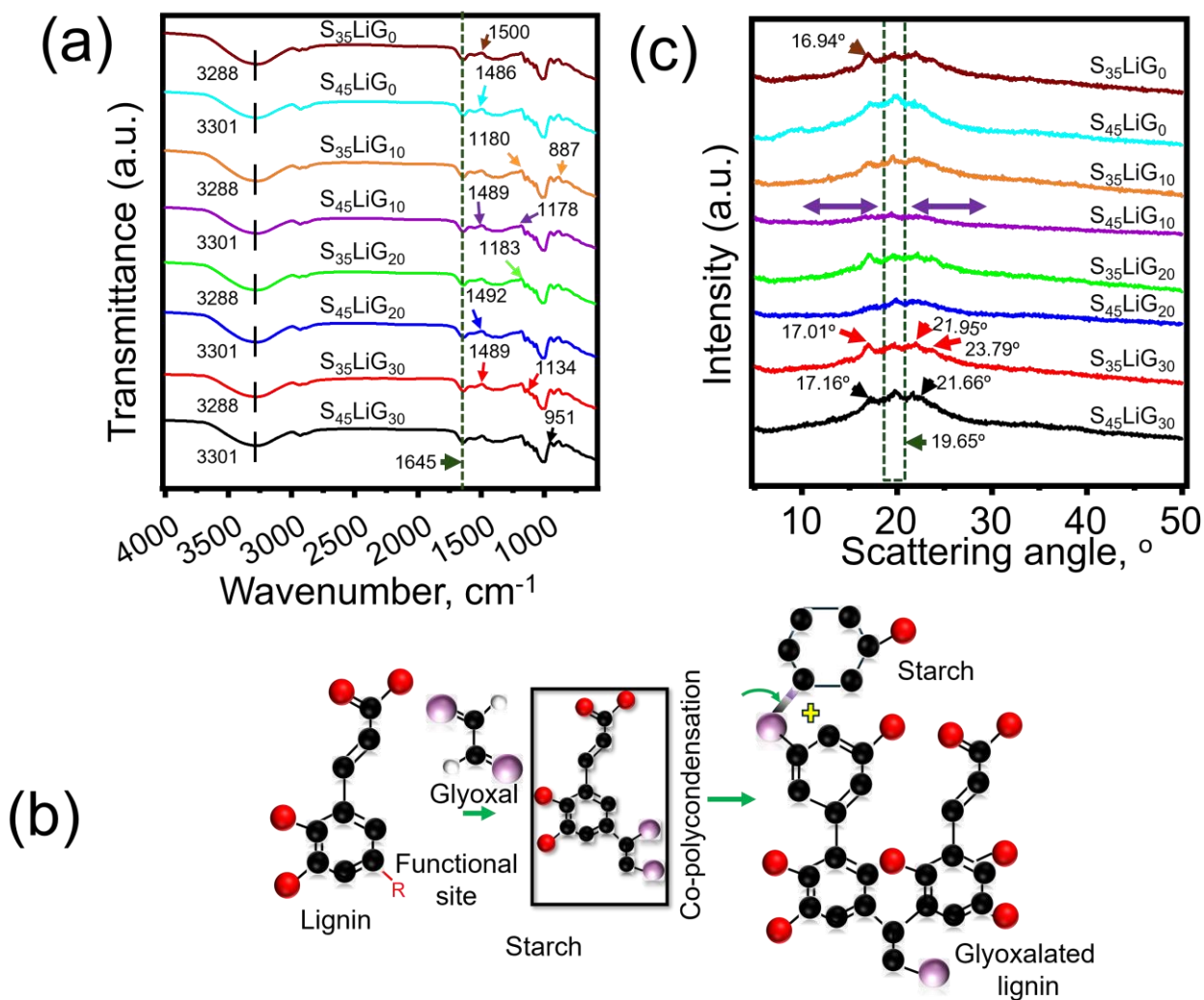


Figure:

3.4. Biofoam morphology

Figure 4 presents the cross-sectional morphology of the biofoam specimens as influenced by varying concentrations of LiG. In the S₃₅ specimens, low-magnification images (white-circled regions) revealed a dense and homogeneous external wall with a predominantly closed cell structure. However, higher magnifications (red-square regions) expose the presence of larger closed cells, a characteristic commonly observed in thermoplastic starch-based foams (Engel et al., 2019; Soykeabkaew et al., 2015). This structural variation is primarily governed by the composition and distribution of LiG within the starch matrix. An increase in LiG concentration results in a noticeable reduction in cell size, leading to a denser morphology. This observation aligns with previously reported density values, suggesting that LiG enhances molecular interactions between starch and lignin, reinforcing the structural integrity of the foam (Luo et al., 2020; Trovagunta et al., 2022). The crosslinking effect of LiG likely restricts gas bubble expansion during foaming, contributing to the formation of smaller, more compact cells. Furthermore, the non-uniform drying pattern characteristic of compression-molded foams plays a significant role in the final morphology. The polymer matrix near the mold surface undergoes rapid moisture loss due to direct heat exposure, restricting expansion and leading to a denser outer layer (Engel et al., 2019; Ho et al., 2012; Kaisangsri et al., 2014). In contrast,

the foam interior retains moisture longer, allowing localized expansion. As water is expelled as vapor, the internal structure experiences uneven swelling, often resulting in cell rupture and increased porosity. The presence of blowing agent facilitates cell formation, though its impact is modulated by the degree of crosslinking induced by LiG. A structural comparison of the foams revealed that S₄₅ specimens lacked uniformly distributed closed cells, unlike the S₃₅ samples, which exhibited a more organized cell arrangement. This discrepancy may be attributed to the reduced viscosity of the batter. The higher starch concentration, combined with limited water availability, likely contributed to pore collapse under compression, a phenomenon particularly evident in the S₄₅LiG₀ sample. Interestingly, the increasing LiG concentration in the S₄₅ formulations appears to marginally improve void formation by modifying the rheology of the starch paste prior to molding. Previous studies have reported that low-viscosity starch pastes struggle to retain vapor bubbles effectively, whereas higher-viscosity pastes can better stabilize the foam structure (Engel et al., 2019; Figueiró et al., 2024; Tapia-Blácido et al., 2022).

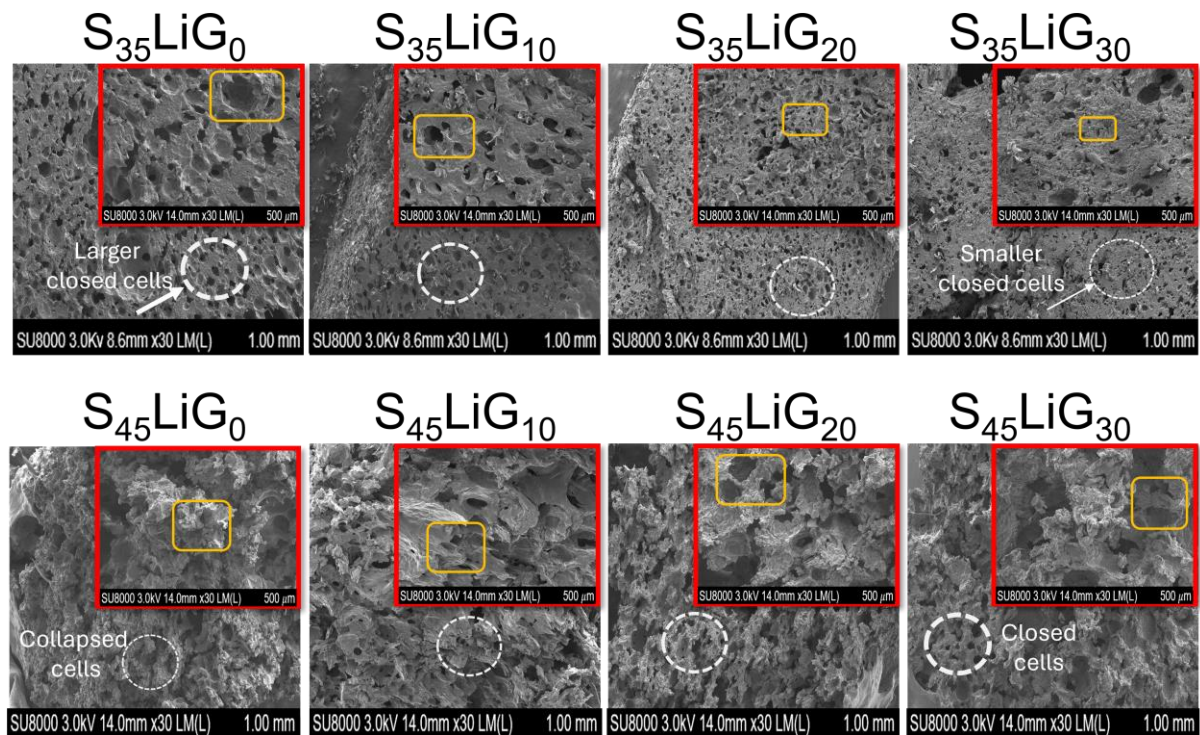


Figure 4:

3.5. Elemental composition

The elemental composition of the biofoams, as determined by Energy Dispersive X-ray (EDX) analysis, confirms that carbon (C) and oxygen (O) are the predominant elements, consistent with the organic nature of starch. Starch is primarily composed of glucose units (C₆H₁₀O₅), making it inherently rich in carbon and oxygen (Bahuguna et al., 2024; Felipe Melo Lima Gomes et al., 2024). The measured carbon content ranges from 49.35% to 57.60%, while oxygen content varies between 33.85% and 47.10%. (Gupta et al., 2020) and (F. Liu et al., 2025) have reported similar range of values. In addition to C and O, minor elements such as sodium (Na, 1.00–1.40%), potassium (K, 0.70–1.00%), and aluminum (Al, 0.35–1.00%) were detected. The presence of Na is likely attributed to the blowing agent, while K and Al may originate from raw materials or be introduced as processing impurities. Other trace elements, including magnesium (Mg), silicon (Si), sulfur (S), and phosphorus (P), appeared in minimal

amounts (<1%), possibly as inherent components of starch, lignin, or additives used in the biofoam formulation. A notably higher Si content (5.40%) was detected in the **S₄₅LiG₁₀** specimen, suggesting potential contamination from silicone-based materials or processing equipment. Furthermore, **S₄₅LiG₁₀** exhibited the highest carbon content (57.60%) and the lowest oxygen content (33.85%), which may be attributed to accelerated polycondensation reactions during compression molding. This process likely induced partial carbonization, leading to the loss of oxygen-containing functional groups (e.g., hydroxyl groups) and an increase in carbon content (Ilić et al., 2022; Qiu et al., 2023), aligning with the observed trend. The elemental distribution of the **S₃₅LiG₀** and **S₄₅LiG₁₀** specimens is illustrated in **Figure 5**, providing further insight into the spatial dispersion of metal atoms within the biofoam structure. This distribution highlights the homogeneous presence of carbon and oxygen, along with the localized accumulation of trace elements, which may influence the mechanical and thermal properties of the biofoams.

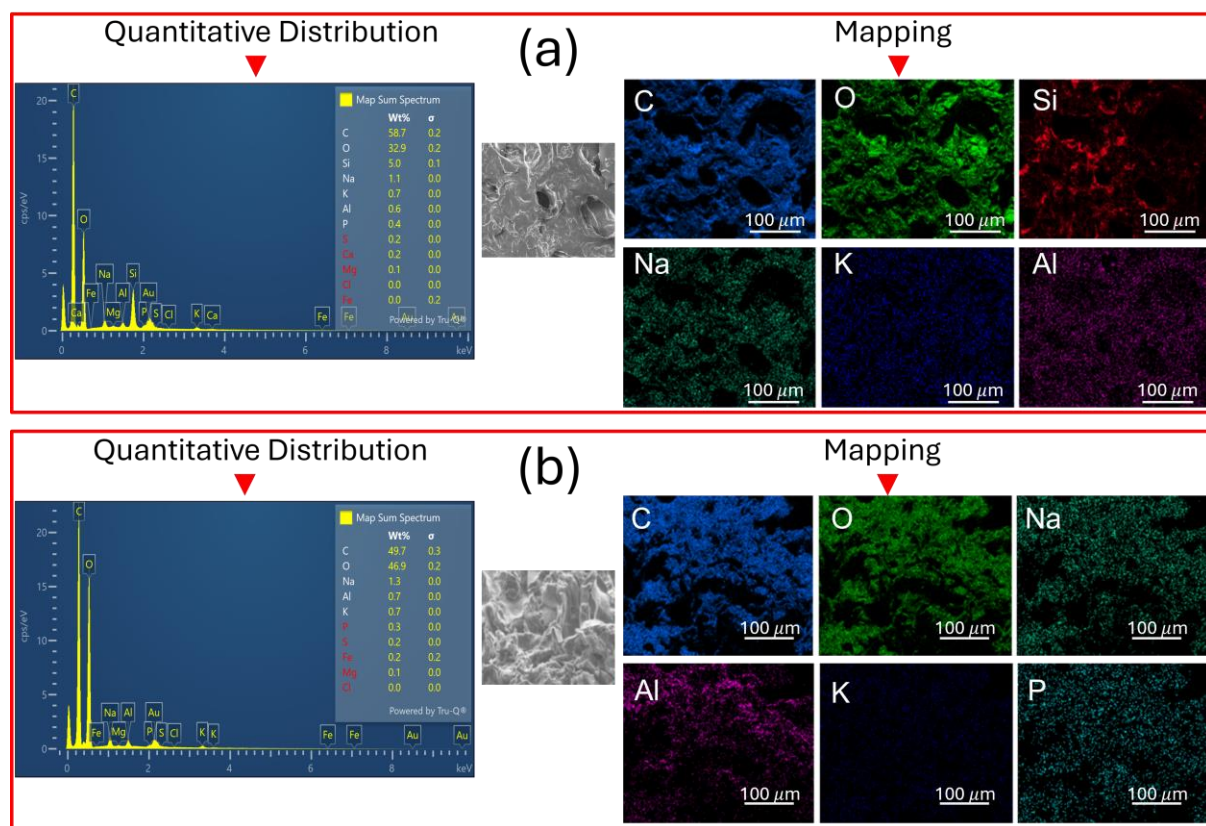


Figure (a) (b)

Table 3: Summarized percentage elemental composition for biofoams obtained from air classified starch with lignin:glyoxal at given loading of LiG (0%, 1%, 2%, and 3%)[†].

Biofoam specimen	Elements										
	C	O	Na	K	Al	Mg	Si	S	P	Fe	Cl
S ₃₅ LiG ₀	49.80±0.14	47.00±0.14	1.40±0.14	0.80±0.14	0.45±0.35	0.10±0.00	X	0.20±0.00	0.25±0.07	0.10±0.14	0.05±0.07
S ₄₅ LiG ₀	49.80±0.42	47.10±0.57	1.30±0.00	0.85±0.07	0.40±0.14	0.10±0.00	0.10±0.00	0.15±0.07	0.30±0.00	X	X

S ₃₅ LiG ₁₀	51.65±0.21	44.45±0.07	1.20±0.00	0.90±0.14	1.00±0.14	0.10±0.00	0.10±0.00	0.20±0.00	0.40±0.00	0.05±0.07	0.10±0.00
S ₄₅ LiG ₁₀	57.60±1.56	33.85±1.34	1.00±0.14	0.70±0.00	0.65±0.07	0.10±0.00	5.40±0.57	0.20±0.2	0.35±0.07	0.10±0.14	0.05±0.07
S ₃₅ LiG ₂₀	50.05±0.21	46.80±0.00	1.40±0.00	0.80±0.14	0.35±0.07	0.10±0.00	X	0.15±0.07	0.35±0.07	0.00±0.00	0.00±0.00
S ₄₅ LiG ₂₀	49.35±0.35	47.40±0.14	1.20±0.00	1.00±0.14	0.55±0.07	X	X	0.15±0.07	0.30±0.00	0.05±0.07	0.10±0.00
S ₃₅ LiG ₃₀	49.95±0.49	46.60±1.13	1.40±0.00	0.80±0.14	0.45±0.07	0.10±0.00	X	0.20±0.00	0.35±0.07	0.15±0.21	0.00±0.00
S ₄₅ LiG ₃₀	51.00±0.14	44.95±0.64	1.30±0.00	0.95±0.07	0.40±0.14	0.10±0.00	0.35±0.07	0.20±0.00	0.40±0.00	0.05±0.07	0.10±0.00

The data are reported as mean ± standard deviation (n=2). “X” represents not detected.

4. Conclusion

Ethics approval and consent to participate

Not Applicable.

Consent for publication

The authors give the outright permission for publication of all data, images, and scientific contributions provided in this research.

CRedit authorship contribution statement

Kehinde James Falua: Conceptualization, literature review, experimentation, analysis, writing—original draft. **Ravi Patel:** Review and editing. **Mostafa Nikkah Dafchachi:** Review and editing. **Amin Babaei-Ghazvini:** Review and editing. **Bishnu Acharya:** Conceptualization, supervision, source for research fund, article review, and edit.

Funding source

This research was funded by the Saskatchewan Ministry of Agriculture - Strategic Research Initiative funds for Pulse Starch Utilization.

Declaration of competing interest

The authors affirm that they possess no identifiable competing financial interests or personal affiliations that could be perceived to have influenced the findings reported in this paper.

Acknowledgements

The authors extend their gratitude to the scientists at the Saskatchewan Structural Sciences Center (SSSC) for their support. Special thanks to Dr. Yongfeng Ai of the Department of Food and Bioproduct Sciences, University of Saskatchewan, Canada, and Mr. Sandeep Yadav are

thanked for providing the faba bean starch, and to Mr. Sandeep Yadav for his assistance with SEM imaging.

Data availability

Data will be made available upon request.

References